A Novel Logarithmic-Spiral-Shaped 3-D-Printed Dielectric Polarizer for Dual-Circularly Polarized Conical-Beam Radiation Patterns in the Ka-Band

Javier Melendro-Jiménez, Pablo Sanchez-Olivares, Adrián Tamayo-Domínguez, Jose Luis Masa-Campos, and José-Manuel Fernández-González, *Senior Member, IEEE*

***Abstract*— In this contribution, the design of a novel logarithmic-spiral-shaped (LSS) anisotropic dielectric polarizer is presented for millimeter-wave applications within the Ka-band (28–30 GHz). The proposed antenna is composed of a conical horn fed by a waveguide dual-mode converter (DMC), where the TE_{01} and TM_{01} modes are independently excited to generate linearly azimuthal polarized and linearly radial polarized conical beam radiation patterns, respectively. The horn antenna is loaded with the novel LSS dielectric polarizer, which converts the linearly azimuthal polarized wave generated by the excitation of the TE_{01} mode into a right-handed circularly polarized (RHCP) wave and the linearly radial polarized wave generated by the excitation of the TM_{01} mode into a left-handed circularly polarized (LHCP) wave. In order to experimentally validate the proposed design, both the DMC along with the conical horn antenna and the novel LSS dielectric polarizer are manufactured by means of distinct 3-D printing techniques. An excellent agreement between simulations and measurements is achieved.**

***Index Terms*— 3-D printing, antenna feeds, circular polarization (CP), horn antennas, microwave antennas.**

I. Introduction

CONICAL-BEAM (CB) antennas have garnered significant attention due to their unique characteristics, making them highly suitable for meeting the escalating demands of enhanced communication systems. These antennas are extensively utilized in the Ka-band for applications, such as indoor 5G NR communications [1] and the burgeoning field of drone applications [2], [3]. Furthermore, they are widely employed in establishing connectivity between terrestrial vehicles in motion and geostationary satellites [4]. In many of these applications, moreover, the feature of circular polarization (CP) proves highly advantageous, as it demonstrates robustness against multipath effects, and it further ensures stability in instances of misalignment between transmitter and receiver. Consequently, recent numerous attempts of achieving CP-CB radiation can be found in the literature. Some designs are based on geometrical solutions [5] and other realizations rely on planar solutions, for instance, by employing printed microstrip antennas while exciting higher order electromagnetic modes. Exciting two orthogonal TM_{21} modes in a circular patch antenna has been proven as an efficient method to generate a CP-CB pattern [6], [7]. Other realizations based on planar patch antennas involve the modification of the patch structure by adding curved conducting branches. By feeding a circular patch at its geometric center with its TM_{01} and TM_{02} modes and optimizing the conducting branches, it is possible to generate electric fields polarized in both radial and azimuthal directions, respectively, with a 90° phase offset, resulting in the generation of a CP-CB pattern [8], [9].

As can be seen, antenna designs presented in the literature that enable the generation of CP-CB radiation patterns predominantly consist of flat printed low-gain antennas operating in low-frequency bands. With the prevailing trend of expanding the frequency spectrum to accommodate emerging applications that demand increased bandwidth capabilities, there is an imperative to propose novel designs of high-gain CP-CB antennas capable of operating in the Ka-band and higher frequencies. Some high-gain linearly polarized (LP) CB antenna designs have recently been proposed to operate within Ka-band frequency spectrum [2], [10]. However, there is still a need for a high-gain CP-CB solution. The generation of high-gain CB radiation can be straightforwardly accomplished employing waveguide technology. By exciting the TE_{01} and TM_{01} modes of a circular waveguide and employing a suitable conical horn antenna, it is possible to achieve two high-gain LP-CB radiation patterns. However, there is a need to convert these dual-LP CB radiation patterns into dual-CP CB radiation patterns. All the presented designs capable of generating CP-CB radiation share the characteristic of addressing the CP generation at the antenna element level, which, in many cases, tends to increase the complexity of the design. As additive manufacturing technologies continue to gain widespread popularity, opportunities arise for designing intricate structures that were traditionally challenging to produce using conventional manufacturing methods [11]. Consequently, the prospect of liberating the antenna element of the task of generating CP in order to simplify its design can be contemplated. Currently, an established method to achieve linear to CP conversion

Manuscript received 7 February 2024; revised 18 May 2024; accepted 8 June 2024. Date of publication 18 June 2024; date of current version 9 August 2024. This work was supported in part by the National Research, Development, and Innovation Program of the Ministry of Economy (Government of Spain) through New Antenna Array Technologies and Digital Processing for Future Integrated Terrestrial and Space Millimeter-Wave Radio Systems Project–UPM-InTerSpaCEInTerSpaCE under Grant PID2020-112545RB-C51; and in part by MCIN/AEI/10.13039/501100011033 under Project PID2020-112545RB-C51. *(Corresponding author: Javier Melendro-Jiménez.)*

The authors are with the Information Processing and Telecommunications Center (IPTC), ETSI Telecomunicación, Universidad Politécnica de Madrid, 28040 Madrid, Spain (e-mail: javier.melendro.jimenez@upm.es; pablo.sanchezo@upm.es; a.tamayo@upm.es; joseluis.masa@upm.es; josemanuel.fernandez.gonzalez@upm.es).

Color versions of one or more figures in this article are available at https://doi.org/10.1109/TAP.2024.3415423.

Digital Object Identifier 10.1109/TAP.2024.3415423

involves the utilization of an anisotropic planar dielectric polarizer comprised of parallel dielectric slabs [12], which enables the conversion of an LP wave into a CP wave. Due to its simplicity and straightforward manufacturability, several antenna designs have adopted this polarization conversion technique for millimeter-wave band applications [13], [14], [15]. This polarizer can be utilized either by placing it away from the feed, where it is illuminated by a radiated electromagnetic field, as implemented in design [13], or by positioning it at the feed aperture, where it is illuminated by an extended electromagnetic mode, as performed in [12]. The latter method allows for the realization of a more compact antenna with the drawback that the electromagnetic field illuminating the polarizer deviates from being a transverse electromagnetic wave, which is the optimal case for achieving the highest polarization purity.

In pursuit of optimal illumination while considering form factor, an alternative method has been proposed, which entails the placement of a dielectric lens between the feed and the polarizer, with the purpose of illuminating the latter with a plane or quasi-plane wave, thus seeking to emulate the TEM wave ideal excitation condition [14], [15]. However, the introduction of a dielectric lens inevitably entails a slight increase in the overall size of the design, along with other undesired effects, such as reflections at the dielectric–air interfaces as well as an increase in overall dielectric losses. Regarding the polarization conversion capability of the planar anisotropic dielectric polarizer, due to the shape and geometric arrangement of the dielectric slabs, the polarizer only exhibits the desired anisotropy to achieve polarization conversion when its excitation is performed with an LP wave with its electric field vectors rectilinearly oriented. In general, electromagnetic modes that enable the generation of CB radiation patterns exhibit electric and magnetic field distributions that do not properly align with the geometry of the traditional dielectric polarizer, as instead of rectilinearly oriented electric field vectors, these modes usually feature radial or azimuthal electric field polarizations, as can be observed in [6], [7], [8], and [9] or in the already mentioned TE_{01} and TM_{01} modes of a circular waveguide. Thus, the traditional dielectric polarizer geometry proves to be inefficient in the conversion of radial or azimuthal polarized electric fields into CP electric fields, as the misalignment of its geometry with the geometry of the field radiated by these higher order modes impedes the generation of the necessary anisotropy for CP conversion. Hence, there is a current need for an innovative polarizer structure capable of converting radial and azimuthal polarized electric fields into CP electric fields, thus achieving a CP-CB radiation pattern from an LP feed.

Acknowledging this necessity, in this contribution, a novel cylindrical dielectric polarizer capable of generating dual-CP CB radiation patterns from a dual-LP antenna feeder is presented for millimeter-wave applications in the Ka-band. As already outlined, the aim is to generate high-gain CB far-field radiation featuring dual-CP. The generation of two CB radiation patterns becomes achievable through the distinctive electromagnetic properties of the TM_{01} and TE_{01} modes of a circular waveguide. These modes exhibit electric field nulls

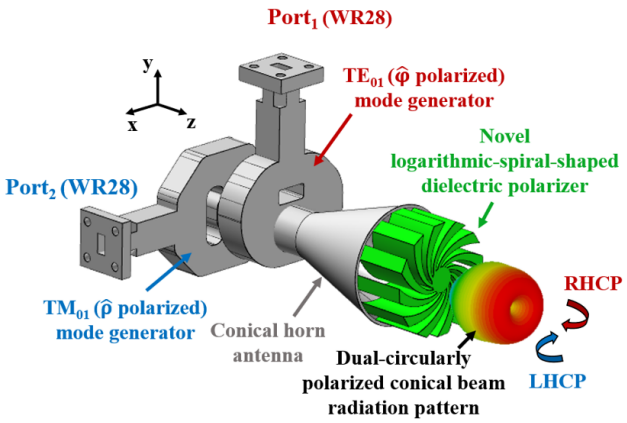

Fig. 1. Proposed antenna design. DCC and integrated LSS dielectric polarizer.

at their center and maxima in the central circular crown of the waveguide. Thus, radiating these modes through a conical horn results in the generation of two far-field CB radiation patterns featuring orthogonal linear polarizations, one radial (TM_{01}) and one azimuthal (TE_{01}). To attain CP in both CB radiation patterns, as previously indicated, the design of a novel dielectric polarizer demonstrating anisotropy in the polarization directions of both modes, radial and azimuthal, is imperative.

This article is organized as follows: Section II is dedicated to detailing the operation of the novel LSS anisotropic dielectric polarizer. A review of the background theory of the traditional dielectric polarizer is conducted, followed by a comprehensive explanation of the operation and design of the new proposed LSS polarizer. In Section III, an experimental design of the proposed LSS polarizer is carried out to validate its operation. TM_{01} and TE_{01} modes are generated by means of a dual-mode converter (DMC), which feeds a conical horn that integrates the proposed LSS dielectric polarizer at its aperture. This experimental design, shown in Fig. 1, is intended to operate in the 28–30-GHz frequency spectrum, although the polarizer may cover a much wider frequency band, as demonstrated in Section II-C. As stated, the DMC enables the excitation of the TE_{01} mode, featuring azimuthal ($\hat{\varphi}$-) polarization, and the TM_{01} mode, featuring radial ($\hat{\rho}$-) polarization, in the conical horn. Conversely, the novel LSS dielectric polarizer ensures the LP-CP conversion of the electric field for both modes, thereby generating two CB far-field radiation patterns featuring dual-CP, RHCP, and left-handed circularly polarized (LHCP), respectively. Section IV is dedicated to review the manufacturing techniques employed to realize the antenna design developed in Section III, alongside validating its performance through measurements in anechoic chamber. Finally, Section V presents the article conclusions.

II. LSS Anisotropic Dielectric Polarizer

In this section, the proposed novel LSS dielectric polarizer is detailed. Initially, before delving into its operation and design intricacies, a section is dedicated to review the operation of the traditional dielectric polarizer [12], aiming to enhance comprehension regarding the functionality of the newly proposed LSS polarizer.

A. Traditional Dielectric Polarizer

Fig. 2(a) illustrates the configuration of the traditional dielectric polarizer design [12], which consists of a series of dielectric slabs with a thickness of w_1, arranged in parallel, and separated by a distance of w_2, having each slab a height of h. The polarizer is tilted 45°, so if a horizontally or vertically polarized wave is decomposed in its two orthogonal components $\vec{E}_{x_{||}}/\vec{E}_{x_\perp}$ and $\vec{E}_{y_{||}}/\vec{E}_{y_\perp}$, respectively, due to the anisotropy that the polarizer exhibits, each of them is affected differently by the dielectric slabs, as the effective dielectric permittivities in each direction, $\varepsilon_{||}$ and $\varepsilon_\perp$, are different. These dielectric permittivities can be calculated as [16]

$$\varepsilon_{||} = m\varepsilon_1 + (1-m)\varepsilon_0 \tag{1}$$

$$\varepsilon_\perp = \frac{1}{m/\varepsilon_1 + (1-m)/\varepsilon_0} \tag{2}$$

where m, the content ratio, is defined as a ratio between variables w_1 and w_2 [$m = w_1/(w_1 + w_2)$]. The variables ε_1 and ε_0 are the relative dielectric permittivities of the dielectric material and air, respectively. This difference in the value of the effective dielectric constants $\varepsilon_{||}$ and $\varepsilon_\perp$ results in a different propagation constant for each component, leading to a different transmission phase across the polarizer. The transmission phase difference between both components can be calculated as a function of h as follows:

$$\Delta\varphi = \frac{2\pi}{\lambda}\left(\sqrt{\varepsilon}_{||} - \sqrt{\varepsilon}_\perp\right)h. \tag{3}$$

Thus, adjusting the polarizer parameters, it is possible to generate a 90° phase shift between both orthogonal electric field components, achieving LP to CP conversion. As shown in Fig. 2(b) and (c), if a conical horn excited with the degenerate and orthogonal TE_{11x} and TE_{11y} modes illuminates the traditional dielectric polarizer, RHCP and LHCP pencil-beam radiation patterns can be achieved, respectively.

B. Logarithmic-Spiral-Shaped (LSS) Dielectric Polarizer Design

Based on the traditional dielectric polarizer, a novel structure is proposed, as shown in Fig. 2(d). The novel dielectric polarizer consists in LSS dielectric slabs, each having a height of h and a thickness denoted by $w_1(\rho)$. The slabs are azimuthally separated from each other by an arc distance $w_2(\rho)$. As can be seen, both the thickness and separation between dielectric slabs are dependent with ρ, being ρ the radial distance from the origin in a standard cylindrical coordinate system. This dependence arises from the fact that the content ratio, m, must be kept constant for any radial distance. Therefore, both the thickness of the dielectric slabs and their separation increase as the radial distance grows. These parameters can be expressed as a function of the content ratio, m, the radial distance, ρ, and the number of dielectric slabs, N_{slabs}

$$\omega_1(\rho) = \frac{2\pi\rho}{N_{slabs}} \cdot m \tag{4}$$

$$\omega_2(\rho) = \frac{2\pi\rho}{N_{slabs}} \cdot (1-m). \tag{5}$$

The polarizer can convert incident $\hat{\varphi}$- and $\hat{\rho}$-LP waves, achieved by the excitation of the $\hat{\varphi}$-polarized TE_{01} mode and the $\hat{\rho}$-polarized TM_{01} mode in the conical horn antenna, into RHCP and LHCP waves, respectively. This innovative design extends the traditional polarizer concept by ensuring that the rotating slab trajectory forms a local angle of 45° with $\hat{\varphi}$ and $\hat{\rho}$ directions, thus ensuring local anisotropy for incident $\hat{\varphi}$- and $\hat{\rho}$-polarized e-field modes. As linearly $\hat{\varphi}$- ($\vec{E}_\varphi$) and $\hat{\rho}$- ($\vec{E}_\rho$) polarized waves impinge on the anisotropic polarizer, if they are decomposed in their respective orthogonal electric field components, $\vec{E}_{\varphi_{||}}/\vec{E}_{\varphi_\perp}$ and $\vec{E}_{\rho_{||}}/\vec{E}_{\rho_\perp}$, each component will exhibit a different propagation constant, as the local effective dielectric permittivities, $\varepsilon_{||}$ and $\varepsilon_\perp$, are different. This will lead to different propagation constants for each component and, consequently, to different transmission phases. Thus, by tuning the polarizer dimensions, it is possible to generate a 90° phase shift between both electric field components, achieving linear $\hat{\varphi}$- and $\hat{\rho}$-polarization to CP conversion, RHCP and LHCP, respectively. It should be noted again, that in order to maintain a constant value for m, the filling factor, along the whole radius of the polarizer (ρ-direction), the dielectric slabs progressively increase their width and the separation between them radially. When the TE_{01} mode is excited in the conical horn antenna, a linearly $\hat{\varphi}$-polarized electric field ($\vec{E}_\varphi$) impinges on the polarizer. The $\vec{E}_\varphi$ field is decomposed in a +45° tilted component ($\vec{E}_{\varphi_{||}}$), locally parallel to the dielectric slabs, and a −45° tilted component ($\vec{E}_{\varphi_\perp}$), locally orthogonal to the dielectric slabs [Fig. 2(d)]. The polarizer will delay the $\vec{E}_{\varphi_{||}}$ component with respect to the $\vec{E}_{\varphi_\perp}$ component. Thus, adjusting the height of the polarizer, a 90° phase difference between these two components can be achieved, obtaining an RHCP wave from a $\hat{\varphi}$-LP one [Fig. 2(e)]. Likewise, when the TM_{01} is excited in the conical horn antenna, a linearly $\hat{\rho}$-polarized electric field ($\vec{E}_\rho$) impinges on the polarizer. The $\vec{E}_\rho$ field is decomposed in a −45° tilted component ($\vec{E}_{\rho_{||}}$), locally parallel to the dielectric slabs, and a +45° tilted component ($\vec{E}_{\rho_\perp}$), locally orthogonal to the dielectric slabs [Fig. 2(d)]. The polarizer Swill delays the $\vec{E}_{\rho_{||}}$ component with respect to the $\vec{E}_{\rho_\perp}$ component. Achieving a 90° phase difference between these two orthogonal components will give rise to an LHCP wave from a linearly $\hat{\rho}$-polarized one [Fig. 2(f)].

Concerning the design of the LSS dielectric polarizer, it has been crafted as follows. As depicted in Fig. 2(d), it features two primary components: a central dielectric hub and several dielectric slabs emanating from it. The primary role of the central hub is to provide structural rigidity. Its placement has been precisely positioned at the geometric center of the polarizer, coinciding with the nulls of the electric and magnetic fields of both TM_{01} and TE_{01} modes at the aperture of the conical horn antenna. This strategic placement ensures the robustness of the polarizer without compromising the propagation of these modes. On the other hand, the polarizing dielectric slabs are designed in accordance with the aforementioned considerations to generate the necessary anisotropy for LP to CP conversion. At each point, the polarizing slab should be tilted 45° to the incident $\hat{\varphi}$- and $\hat{\rho}$-polarized electric fields. The analytical expression that enables the depiction of the profile that satisfies the condition of maintaining a constant angle with

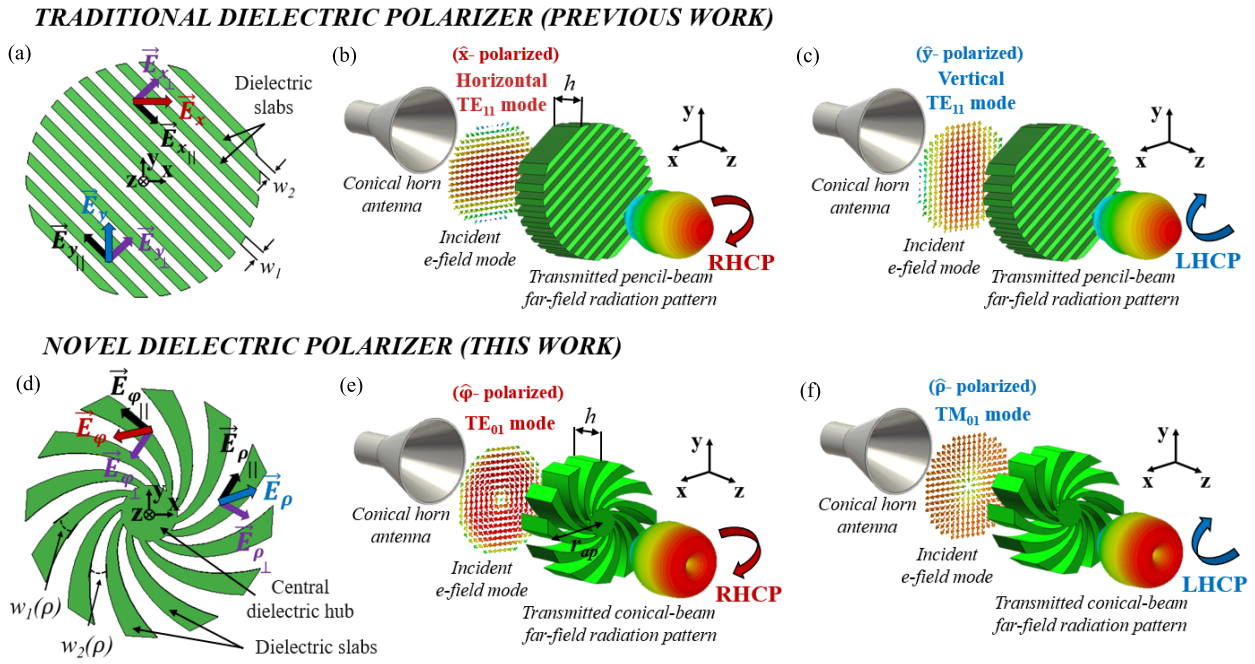

Fig. 2. (a) Front view of traditional dielectric polarizer [12], (b) traditional dielectric polarizer [12]: $\hat{x}$-polarized TE_{11} mode—RHCP conversion, (c) traditional dielectric polarizer [12]: $\hat{y}$-polarized TE_{11} mode—LHCP conversion, (d) front view of novel LSS dielectric polarizer, (e) novel LSS dielectric polarizer: $\hat{\varphi}$-polarized TE_{01} mode—RHCP conversion, and (f) novel LSS dielectric polarizer: $\hat{\rho}$-polarized TM_{01} mode—LHCP conversion.

the unit vectors $\hat{\varphi}$- and $\hat{\rho}$- throughout its entire trajectory is that of a logarithmic spiral. This expression can be presented in polar coordinates as follows [17]:

$$\rho_{slab}(\varphi) = r_{ap} \cdot e^{-\varphi \cot \alpha} \tag{6}$$

being ρ_{slab} the ρ coordinates of the dielectric slab's profile, r_{ap} the radius of the conical horn aperture, φ the azimuthal angle, and α the angle between the trajectory of the spiral profile at any point, denoted as $\hat{r}_{slab}$, and the unit vector $\hat{\rho}$- at that same point. Thus, the profile that the dielectric slab should have to generate the necessary anisotropy for the transformation of the incident LP $\hat{\varphi}$- and $\hat{\rho}$-polarized electric fields into CP fields, shown in Fig. 3(a), is determined using (6) with $r_{ap} = 20$ mm and $\alpha = 45°$, as selecting this value for α ensures that the logarithmic spiral trajectory forms a 45° angle with both $\hat{\varphi}$- and $\hat{\rho}$-directions at all points of its profile. An infinitesimal close-up view of the dielectric slab profile is shown in Fig. 3(b). As can be seen, at every generic angle φ_i, the trajectory of the dielectric slab, $\hat{r}_{slab}(\varphi_i)$, is tilted 45° to the orientation of the incident electric fields, $\hat{\varphi}(\varphi_i)$ and $\hat{\rho}(\varphi_i)$. Following (4) and fixing values for N_{slabs} and m, a second profile can be outlined to comply with the calculated dielectric slab's width [Fig. 3(c)]. Subsequently, following (5) with the same previously fixed values for N_{slabs} and m, the separation between dielectric slabs can be computed, leading to the final LSS polarizer observed in Fig. 3(d).

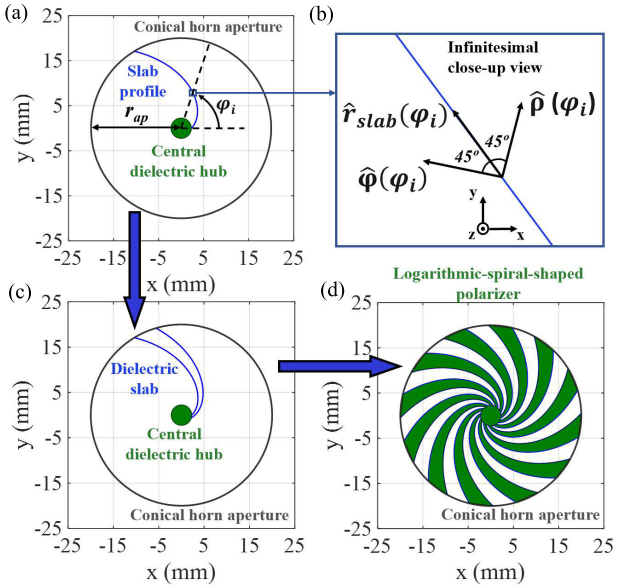

Fig. 3. Novel dielectric polarizer construction. (a) Dielectric slab profile: logarithmic spiral depicted using (6) with $r_{ap} = 20$ mm and $\alpha = 45°$, (b) close-up (infinitesimal) view of slab profile, (c) dielectric slab surface, and (d) LSS dielectric polarizer.

C. LSS Polarizer Bandwidth Analysis

This section is dedicated to analyze the bandwidth within the Ka-band (26–40 GHz), in which the LSS polarizer exhibits robust operation, allowing for polarization conversion in its two operating modes simultaneously, TE_{01}-RHCP and TM_{01}-LHCP.

Fig. 4 illustrates the simultaneous dual-mode operation of the LSS polarizer in the Ka-band, with axial ratio simulated results extracted from *CST Microwave Studio* software. The simulation method consisted in directly exciting the TE_{01} and TM_{01} modes on a conical horn with the integrated LSS dielectric polarizer at its aperture. A parametric variation of the variable h is performed for a fixed value of $m = 0.5$ and a high value for N_{slabs}, which ensures the LSS polarizer to exhibit a homogeneous anisotropy along its entire aperture, thus guaranteeing optimal polarization conversion capabilities.

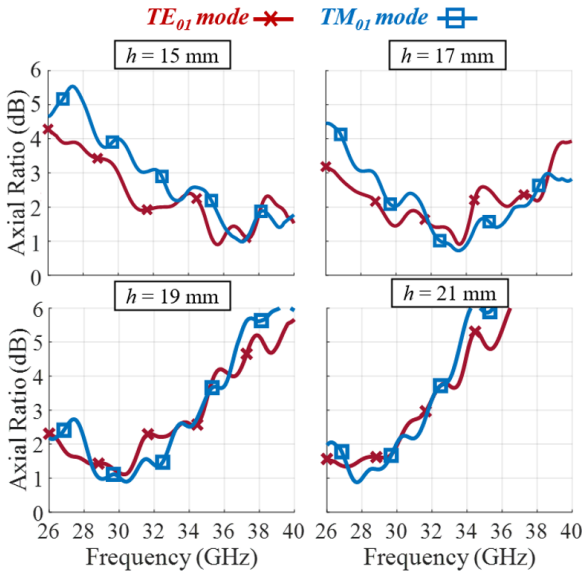

Fig. 4. Wideband operation of the LSS polarizer within the Ka-band. Dual-mode axial ratio for different values of h.

As seen, by adjusting the value of h, the height of the LSS polarizer, it is straightforward to select the subband within the Ka-band, wherein the LSS polarizer can operate robustly in its dual-mode configuration. The relative bandwidth in terms of axial ratio (AR $<$ 3 dB) is about 35% for TE_{01} mode and 30% for TM_{01} mode. It can be observed that for higher values of h, the LSS polarizer operates in the lower part of the Ka-band, whereas reducing the value of h enables operation in the upper part of the Ka-band.

III. Experimental Design: DMC and Conical Horn With Integrated LSS Polarizer

This section is dedicated to develop a fully functional antenna within the 28–30-GHz frequency band, previously depicted in Fig. 1. As mentioned, the experimental antenna proposal consists of a DMC and the novel LSS dielectric polarizer. The DMC enables the excitation of the TE_{01} mode, featuring azimuthal ($\hat{\varphi}$-) polarization, and the TM_{01} mode, featuring radial ($\hat{\rho}$-) polarization, in a conical horn. The novel LSS dielectric polarizer is integrated into the conical horn aperture to ensure the LP-CP conversion of the electric field for both modes, achieving dual-CP CB radiation. For this purpose, a first parametric analysis of all the LSS polarizer geometric parameters is conducted in Section III-A to optimize its dual-mode performance in the specified frequency range, followed by the DMC and conical horn design in Section III-B, which is also optimized to operate in the 28–30-GHz frequency band. It is important to note that, as will be shown in this section, the DMC limits the operational bandwidth of the complete antenna in terms of impedance matching, yet as stated in Section II-C, the novel LSS polarizer exhibits a wider operational frequency range in terms of polarization conversion capabilities.

A. LSS Polarizer Simulated Parametric Analysis

Regarding the variables defining the optimal dimensions of the dielectric LSS polarizer, a parametric analysis is conducted through electromagnetic simulation using CST Microwave Studio as the electromagnetic simulation tool. The simulation method involved directly exciting the TE_{01} and TM_{01} modes on the circular waveguide that feeds the conical horn with the integrated LSS dielectric polarizer at its aperture. The parametric analysis of the LSS polarizer variables is depicted in Fig. 5. Initially, an in-depth examination of the variations in parameters h and m is conducted across three specified frequencies within the band, namely, 28, 29, and 30 GHz, while maintaining N_{slabs} at a constant value of 12. Both parameters, h and m, are instrumental in achieving maximal polarization purity within our designated frequency range. Concurrently, the variable N_{slabs} assumes a critical role in homogenizing the anisotropy exhibited by the LSS polarizer at its aperture, allowing for a better polarization conversion of the electric field distributions of the TM_{01} and TE_{01} modes. Thus, Fig. 5(a)–(c) delineates the axial ratio variations for distinct combinations of h and m at the aforementioned frequencies. Notably, optimal axial ratio values manifest at medium values of m, ranging between 0.4 and 0.5. Conversely, parameter h assumes greater influence in positioning the minimum axial ratio within the desired frequency band. Thus, for lowest in-band axial ratio, h = 19.15 mm and m = 0.5 are selected as optimal values. Following this, the axial ratio for these h and m optimal values is examined for different values of N_{slabs} within the operational frequency range [Fig. 5(d)]. As can be observed, by increasing the value of N_{slabs} while maintaining the optimal values of h and m, the polarizer exhibits a more homogeneous anisotropy along its aperture, resulting in an improved in-band axial ratio. The lowest number of slabs that allows the achievement of the optimal anisotropy homogeneity and, therefore, the optimal axial ratio in the design frequency band, is N_{slabs} = 12. Although a higher value of N_{slabs} also enables achieving adequate dual-mode polarization conversion, this result is set as optimal as it also ensures the manufacturability of the LSS polarizer. Thus, the optimal parameter configuration for the LSS polarizer is found for h = 19.15 mm, m = 0.5, and N_{slabs} = 12. It is worth mentioning that, while the optimal polarizer height obtained through electromagnetic simulation is h = 19.15 mm, if the calculation is performed making use of the analytical expressions (1)–(3), a discrepancy is observed in the obtained results. With the selected optimal value m = 0.5 and considering that $\varepsilon_1 = 2.7$ for gray resin, which is the material used for the LSS polarizer manufacture, and $\varepsilon_0 = 1$ for air, the calculated values for $\varepsilon_{||}$ (1) and $\varepsilon_{\perp}$ (2) are 1.85 and 1.46, respectively. Thus, an analytical height value of h = 17 mm is calculated with (3) for the polarizer to generate a 90° phase shift between orthogonal electric field components at the central frequency of the band, 29 GHz, achieving LP-CP conversion. This result slightly deviates from the electromagnetically simulated optimal value of h = 19.15 mm, as the electromagnetic simulation considers effects omitted in the theoretical calculation. These include dielectric losses and edge effects in the dielectric slabs as well as reflections at the dielectric–air interfaces. Moreover, the electromagnetic field distributions given by the TM_{01} and TE_{01} modes that impinge on the polarizer differ from being TEM

waves, as assumed in the analytical approach and considered as the optimal scenario in terms of polarization conversion efficiency. This is, indeed, one of the notable advantages of the design. The polarizer is designed to be integrated at the conical horn aperture, ensuring a good polarization purity, even in the absence of optimal feeding by a radiated TEM or quasi-TEM wave.

B. Feed Antenna: DMC and Integrated Conical Horn

Regarding the DMC used to feed the conical horn antenna, as previously mentioned, it is designed based on works [18] and [19], integrating these single-mode converters (SMC) into a single-piece DMC used to feed a conical horn antenna [Fig. 6(a)]. Since this does not constitute a novel contribution, a detailed explanation of its operation is not provided, as it is already covered in the original works. However, to demonstrate the proper functioning of the conical horn antenna [Fig. 6(b)] and the successful excitation of TE_{01} [Fig. 6(c)] and TM_{01} [Fig. 6(d)] modes, its simulated radiation properties are analyzed with the commercial electromagnetic software *CST Microwave Studio*. The DMC features two input ports, which are standard WR28 rectangular waveguides. As can be seen from Fig. 6(c), TE_{10} mode is excited at port 1 to generate the TE_{01} mode inside the output circular waveguide, which exhibits a $\hat{\varphi}$-polarized electric field. Conversely, as seen in Fig. 6(d), TE_{10} mode is excited at port 2 to generate the TM_{01} mode inside the output circular waveguide, which exhibits a $\hat{\rho}$-polarized electric field. As observed in Fig. 6(e), both modes are adequately excited within the operational bandwidth, as their reflection coefficient remains below -15 dB throughout most of the frequency band. Concerning the radiation properties of the conical horn antenna, TE_{01} [Fig. 6(f)] and TM_{01}[Fig. 6(g)] directivity patterns are shown at the central frequency of the band, 29 GHz. As can be seen, the antenna successfully achieves the generation of two CB radiation patterns featuring orthogonal LP. It is worth noting that the radiation pattern generated by the TM_{01} mode demonstrates higher directivity than the radiation pattern generated by the TE_{01} mode. The TM_{01} mode exhibits a more uniform field distribution at the horn aperture than that of the TE_{01} mode, which presents a tapered field distribution with nulls both at the center and edges of the horn aperture. Consequently, the CB pattern radiated by the excitation of the TM_{01} mode in the conical horn antenna features higher directivity, along with slightly higher secondary lobes, typical of uniformly illuminated aperture antennas.

The antenna, comprised by the DMC with the integrated conical horn and the LSS polarizer, exhibits a total relative bandwidth of dual-mode operation that is limited by the relative bandwidth of the DMC in terms of impedance matching. Defining a maximum reflection coefficient of -10 dB, the TE_{10}–TE_{01} mode converter exhibits a relative bandwidth of 10.1%, whereas the one for the TM_{10}–TE_{01} is slightly higher, specifically of 13.7%. Furthermore, as demonstrated in this section, both mode converters exhibit a reflection coefficient below -14 dB across the entire operating band, from 28 to 30 GHz, which corresponds to an operational bandwidth of 6.9%. However, it is crucial to emphasize that, even though the operational bandwidth of the entire antenna system is constrained by the relative bandwidth in terms of impedance matching of the DMC, the novel LSS polarizer, as shown in Section II-C, can provide a wider dual-mode relative bandwidth in terms of axial ratio (AR $<$ 3 dB) of about 35% and 30% for TE_{01} and TM_{01} modes, respectively.

IV. Manufacturing and Experimental Results

In this section, an overview of the manufacturing process for the two integral components of the antenna, namely, the DMC and the integrated LSS dielectric polarizer, is provided. Furthermore, a comparative analysis is presented between the experimental results of the antenna and the outcomes of the electromagnetic simulations.

Regarding the manufacturing process, the DMC and the conical horn antenna are produced as a single piece using AlSi10Mg alloy through selective laser melting (SLM) technology. SLM represents a state-of-the-art additive manufacturing method, in which fine layers of metal powder are selectively melted and fused using a high-powered laser. This method, operating in a layer-by-layer fashion, allows for the construction of intricate microwave components tailored for millimeter-wave band applications [20], [21], [22]. Conversely, the LSS dielectric polarizer is additively manufactured using photopolymer resin. Specifically, the stereolithography (SLA) 3-D printing technique is employed, which utilizes a high-precision laser to selectively solidify a liquid photopolymer resin, layer by layer, thereby enabling the fabrication of complex dielectric structures [11], [13], [14]. The polarizer is printed with the Form 3 3-D printer using gray resin material, both supplied by Formlabs. Thus, the characterization of gray resin dielectric properties is carried out employing waveguide measurement techniques. The results yield values for its relative permittivity (ε_r) of 2.7 and a loss tangent ($\tan\delta$) of 0.02. These findings closely align with the values reported in existing [23], [24]. In Fig. 7(a), the complete antenna assembly is shown, consisting in the DCM alongside the conical horn and the integrated LSS dielectric polarizer. Besides, the DMC and the integrated conical horn antenna, manufactured as a single piece by means of SLM, are shown in [Fig. 7(b)]. Additionally, the novel LSS dielectric polarizer, produced through SLA with optimal parameters of $N_{slabs} = 12$, $h = 19.15$ mm, and $m = 0.5$, is shown in Fig. 7(c).

Regarding the experimental results of the prototype, first, the reflection coefficient is shown in Fig. 8. As observed, the measured values are in accordance with the simulated results. The measured reflection coefficients are kept below -10 dB for both modes of operation across the entire operating bandwidth. A resonance in the measured reflection coefficient of the TE_{01} mode at the frequency of 29.4 GHz is observable. This resonance, not present in the simulation, is attributed to minor errors in the DMC's manufacturing process, aspect that is further detailed later in this section. The prototype has also been measured in anechoic chamber to validate its radiation performance. The normalized radiation pattern and the axial ratio are depicted in Fig. 9 for both operating modes, TE_{01} (RHCP) and TM_{01} (LHCP), at the frequencies of 28,

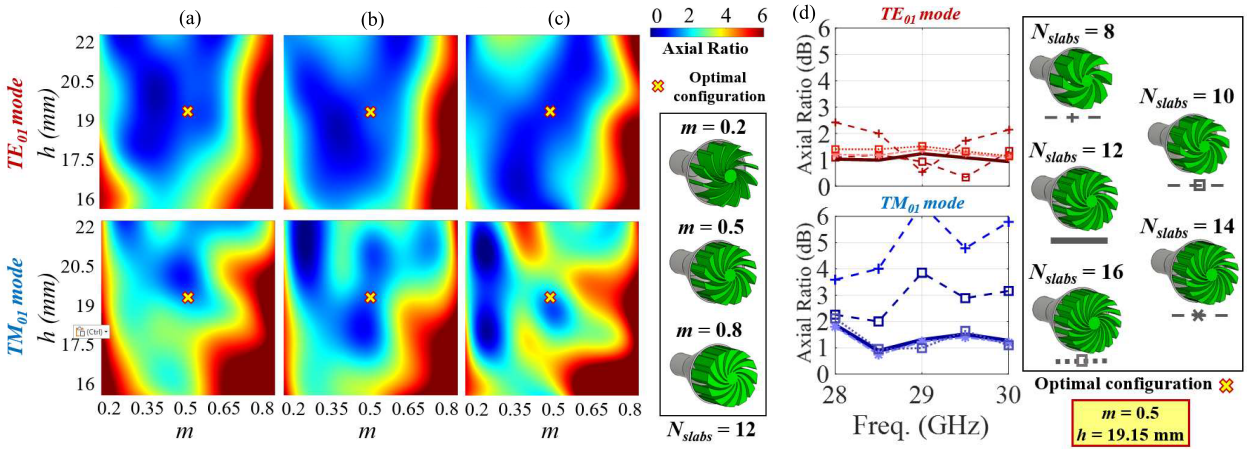

Fig. 5. Simulated parametric analysis of the variables h, m, and N_{slabs} conducted on the conical horn model with the integrated novel LSS dielectric polarizer, directly exciting TE_{01} and TM_{01} modes on the circular waveguide. h and m variation effect on axial ratio for TE_{01} mode (up) and TM_{01} mode (down) for fixed $N_{slabs} = 12$ at (a) 28 GHz, (b) 29 GHz, (c) 30 GHz, and (d) N_{slabs} variation effect on TE_{01} and TM_{01} modes axial ratio for fixed optimal h = 19.15 mm and m = 0.5.

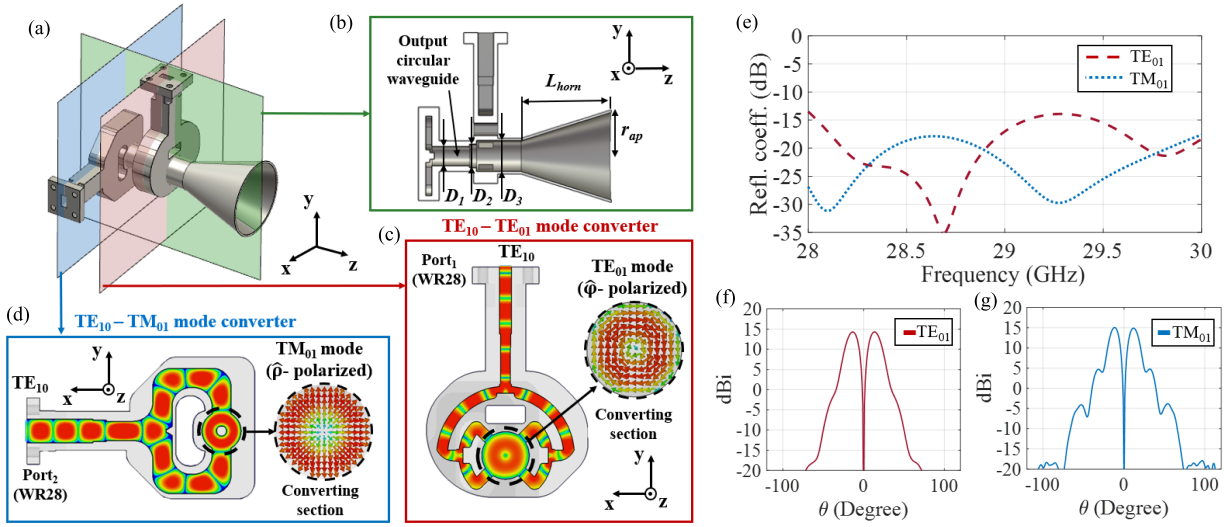

Fig. 6. Overview and radiation performance of the proposed feeder. (a) DCC and conical horn antenna and (b) cross-sectional view: output circular waveguide and horn aperture. Dimensions (mm). $D_1 = 8.8$, $D_2 = 10.8$, $D_3 = 14.2$, $L_{horn} = 41$, and $r_{ap} = 20$, (c) cross-sectional view: TE_{10}—TE_{01} mode converter, (d) cross-sectional view: TE_{10}—TM_{01} mode converter, (e) reflection coefficients for both modes of operation, TE_{01} and TM_{01}, (f) horizontal plane ($\varphi = 0°$) directivity for TE_{01} mode of operation at 29 GHz, and (g) horizontal plane ($\varphi = 0°$) directivity for TM_{01} mode of operation at 29 GHz.

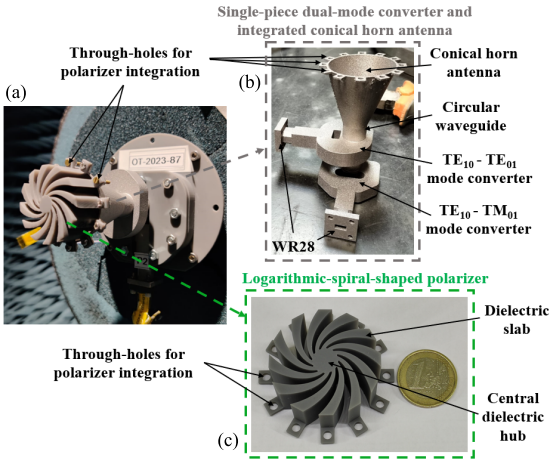

Fig. 7. (a) DCC and conical horn antenna with integrated LSS dielectric polarizer, (b) SLM manufactured DCC and conical horn antenna, and (c) 3-D-printed SLA novel LSS dielectric polarizer.

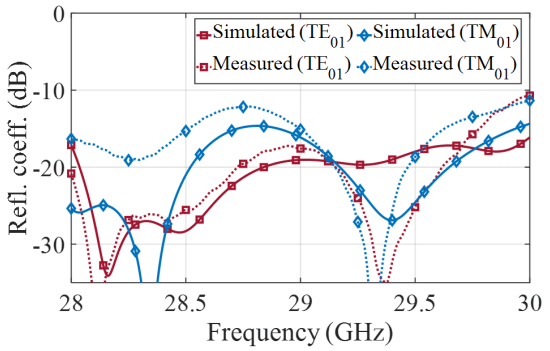

Fig. 8. Simulated versus measured reflection coefficient for both modes of operation, TE_{01} (RHCP) and TM_{01} (LHCP).

29, and 30 GHz for various φ cuts: 0°, 22.5°, 45°, 67.5°, 90°, 112.5°, and 135°, in order to evaluate the rotational symmetry of the dual-CP-CB radiation patterns, both in terms of directivity and axial ratio. First, regarding the normalized radiation pattern, as observed, there is a notable agreement between simulations and measurements. The radiation pattern exhibits its maximum for the TE_{01} (RHCP) configuration at $\theta = 11°$ for 28 and 29 GHz and at $\theta = 10°$ for 30 GHz.

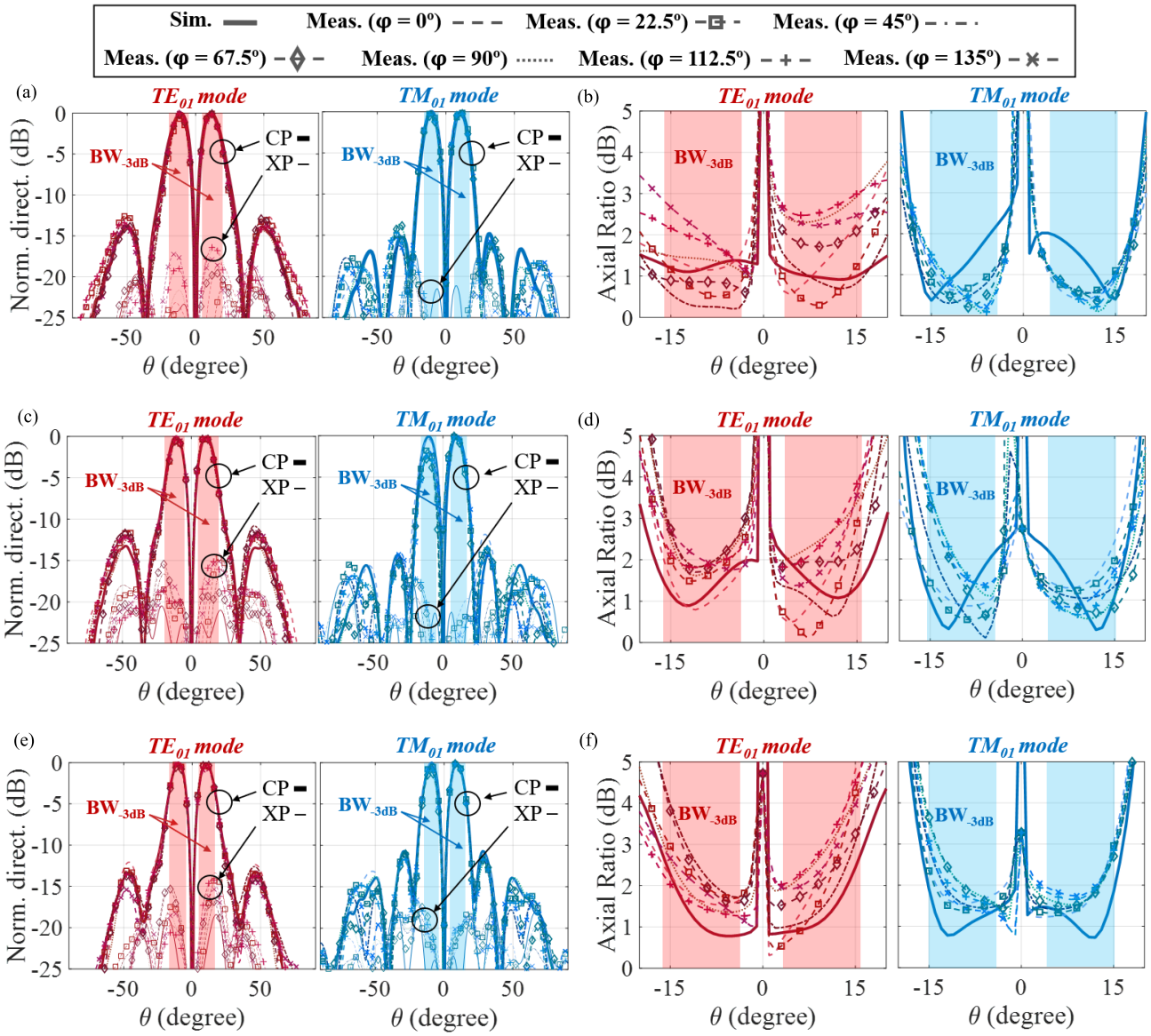

Fig. 9. Simulated versus measured directivity and axial ratio. (a) TE_{10} (RHCP) and TM_{01} (LHCP) normalized directivity at f = 28 GHz, (b) TE_{10} (RHCP) and TM_{01} (LHCP) axial ratio at f = 28 GHz, (c) TE_{10} (RHCP) and TM_{01} (LHCP) normalized directivity at f = 29 GHz, (d) TE_{10} (RHCP) and TM_{01} (LHCP) axial ratio at f = 29 GHz, (e) TE_{10} (RHCP) and TM_{01} (LHCP) normalized directivity at f = 30 GHz, and (f) TE_{10} (RHCP) and TM_{01} (LHCP) axial ratio at f = 30 GHz.

Conversely, for the TM_{01} (LHCP) configuration, the maximum value of the radiation pattern is located at $\theta = 11°$ for 28 GHz, $\theta = 10°$ for 29 GHz, and $\theta = 9°$ for 30 GHz. On the other hand, regarding the CP purity, a significant agreement between simulated and measured results is also observed. The measured axial ratio for both cases remains below 3 dB across the entire operating frequency band in most of the BW_{-3dB}. The measured axial ratio at the maximum value of the main lobe is below 2.5 dB for the TE_{01} mode and below 2 dB for the TM_{01} mode throughout the entire operating band. It is worth mentioning that, while the simulated results for axial ratio and normalized radiation patterns exhibit nearly revolution symmetry, slight asymmetries are observed in the measured results. This discrepancy is attributed to manufacturing errors in the DCM. SLM requires orienting the part to be manufactured in a specific manner to ensure proper fabrication, which can potentially result in asymmetries in the manufactured prototype. These asymmetries, consequently, may lead to resonances at certain frequencies that asymmetrically affect the radiation of the manufactured antenna.

Finally, the directivity and realized gain are depicted in Fig. 10 for both operating modes of the antenna. As observed, there is a strong correspondence between simulations and measurements. It can be noticed that the directivity and gain of the TM_{01} mode (LHCP) are slightly higher than those of the TE_{01} mode (RHCP). As mentioned in Section III-B, the TM_{01} mode exhibits a more uniform field distribution at the horn aperture than that of the TE_{01} mode. Consequently, the CB radiation pattern generated by the TM_{01} mode excitation exhibits higher directivity, as well as higher secondary lobes. The measured in-band directivity ranges from 14.65 to 15.3 dBi for the TE_{01} mode, whereas for the TM_{01} mode, the in-band directivity values are in between 15.7 and 16.1 dBi. Total losses range between 1.7 and 2.1 dB for both

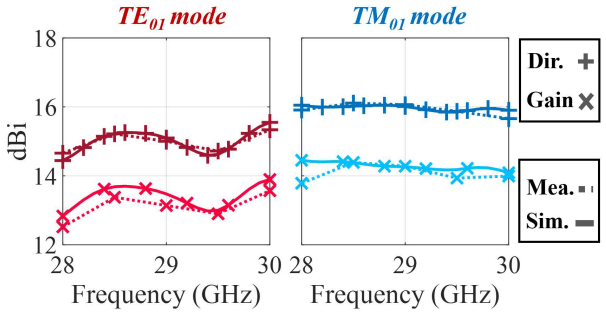

Fig. 10. Simulated versus measured directivity and realized gain for both modes of operation: TE_{01} (RHCP) and TM_{01} (LHCP).

TABLE I
COMPARISON BETWEEN CP-CB ANTENNAS FOUND IN THE STATE OF THE ART

	[5]	[6]	[8]	[2]	This work
Antenna type	Slot array	Printed patch	Printed patch	Monopole + reflectors	Horn antenna
Antenna aperture size**	$0.64\lambda_0$*'	Ø$0.63\lambda_0$	Ø$0.277\lambda_0$	$4.53\lambda_0$ x $4.53\lambda_0$	Ø$3.88\lambda_0$
Polarization	LHCP	RHCP/ LHCP	LHCP	Vertical	RHCP/ LHCP
CP generation	Element level	Element level	Element level	-	Polarizer
Freq. (GHz)	5.7	2.63	1.485	28.3	29
Max. Dir. (dBi)	6.7*	6.86*	2.31	9.05*	15.3/16.1
Max. Real. Gain (dBi)	5.8	6.5	-0.4	8.51	13.6/14.1
AR BW (< 3dB) (%)	8.62	2.28*	3.37	-	35/30
Complexity	High	Low	Low	Medium	Low
Main beam angle (deg.)	45	46	90	22	11/10

*: Not provided. Estimated.
**λ_0 is the free-space wavelength at the band central frequency
*' aperture over elevation plane

TE_{01} and TM_{01} configurations, values that are in accordance with other experimental studies conducted using gray resin as the manufacturing material [25]. In simulations, the loss tangent for gray resin is set to 0.02 for the whole frequency band, as mentioned earlier, while the conductivity set for the AlSi10Mg alloy is 3 MS/m, value that coincides with other studies where the same alloy is employed [26], [27].

To conclude, Table I provides a comparison between the CP-CB antenna presented in this study and other state-of-the-art CP-CB antenna designs. Some of them are characterized by geometrical solutions, such as the truncated cone slot array presented in [5] or by their planar printed structure, such as works presented in [6] and [8], although all of them yield modest gains in low-frequency bands. Conversely, there are proposals for high-gain antennas intended for operation in the Ka-band, as seen in [10], though featuring LP radiation. The presented design incorporates the appealing features of high-gain and a dual CP-CB radiation pattern, highly desirable for addressing the demands of emerging Ka-band applications. Furthermore, by externalizing the polarization conversion task to a 3-D-printed polarizer instead of implementing it at the element level, the design complexity is significantly reduced.

V. CONCLUSION

A novel LSS dielectric polarizer is presented to achieve dual-CP-CB radiation in the Ka-band. The proposed antenna is composed of a waveguide DMC that excites the TE_{01} and TM_{01} modes in a circular waveguide that feeds a conical horn antenna when exciting the TE_{10} mode at its input ports 1 and 2, respectively. The conical horn antenna is loaded with the proposed novel LSS dielectric polarizer. The polarizer, positioned at the conical horn aperture, turns the linearly $\hat{\varphi}$-polarized wave of the extended TE_{01} mode into an RHCP wave and the linearly $\hat{\rho}$-polarized wave of the extended TM_{01} mode into an LHCP wave. Thus, when exciting TE_{10} at port 1, a high-gain RHCP-CB radiation pattern is generated, whereas if the TE_{10} mode is excited at port 2, a high-gain LHCP-CB radiation pattern is generated. The relative bandwidth achieved by the LSS polarizer in terms of axial ratio (AR $<$ 3 dB) is about 35% for TE_{01} mode and 30% for TM_{01} mode.

REFERENCES

[1] B. Feng, J. Lai, L. Li, C.-Y.-D. Sim, L. Deng, and X. Ding, "A dual-polarized shared-aperture antenna with conical radiation patterns and high gain for 5G millimeter-wave ceiling communications," *IEEE Trans. Antennas Propag.*, vol. 71, no. 3, pp. 2278–2289, Mar. 2023.

[2] D. A. Pham, M. Lee, and S. Lim, "High-gain conical-beam planar antenna for millimeter-wave drone applications," *IEEE Trans. Antennas Propag.*, vol. 69, no. 10, pp. 6959–6964, Oct. 2021.

[3] X. Yang et al., "Joint microwave and millimeter-wave antenna design for UAV-enabled communications," *IEEE Trans. Ind. Informat.*, vol. 19, no. 11, pp. 10739–10750, Nov. 2023.

[4] J. Yang, S.-S. Qi, W. Wu, and D.-G. Fang, "A novel high-gain sum and difference conical beam-scanning reflector antenna," *IEEE Access*, vol. 8, pp. 103291–103300, 2020.

[5] G. Chenhu et al., "Truncated circular cone slot antenna array that radiates a circularly polarized conical beam," *IEEE Antennas Wireless Propag. Lett.*, vol. 16, pp. 2574–2577, 2017.

[6] X. Bai, X. Liang, M. Li, B. Zhou, J. Geng, and R. Jin, "Dual-circularly polarized conical-beam microstrip antenna," *IEEE Antennas Wireless Propag. Lett.*, vol. 14, pp. 482–485, 2015.

[7] X. Chen, G. Fu, S.-X. Gong, Y.-L. Yan, and Z.-Y. Zhang, "Single-feeding circularly polarized TM_{21}-mode annular-ring microstrip antenna for mobile satellite communication," *Prog. Electromagn. Res. Lett.*, vol. 20, pp. 147–156, 2011.

[8] B. C. Park and J. H. Lee, "Omnidirectional circularly polarized antenna utilizing zeroth-order resonance of epsilon negative transmission line," *IEEE Trans. Antennas Propag.*, vol. 59, no. 7, pp. 2717–2721, Jul. 2011.

[9] W. Lin and H. Wong, "Circularly polarized conical-beam antenna with wide bandwidth and low profile," *IEEE Trans. Antennas Propag.*, vol. 62, no. 12, pp. 5974–5982, Dec. 2014.

[10] Q. Shi-Shan, Z. Keren, and W. Wen, "Compact Ka-band conical beam filtenna," *IET Microw., Antennas Propag.*, vol. 17, no. 3, pp. 208–215, Feb. 2023.

[11] F. Calignano et al., "Overview on additive manufacturing technologies," *Proc. IEEE*, vol. 105, no. 4, pp. 593–612, Apr. 2017.

[12] K. X. Wang and H. Wong, "A wideband millimeter-wave circularly polarized antenna with 3-D printed polarizer," *IEEE Trans. Antennas Propag.*, vol. 65, no. 3, pp. 1038–1046, Mar. 2017.

[13] J. Melendro-Jimenez, P. Sanchez-Olivares, A. Tamayo-Dominguez, X. Sun, and J. M. Fernandez-Gonzalez, "3D printed directive beam-steering antenna based on gradient index flat lens with an integrated polarizer for dual circular polarization at W-band," *IEEE Trans. Antennas Propag.*, vol. 71, no. 1, pp. 1059–1064, Jan. 2023.

[14] C. Ding and K.-M. Luk, "Wideband omnidirectional circularly polarized antenna for millimeter-wave applications using conformal artificial anisotropic polarizer," *IEEE Trans. Antennas Propag.*, vol. 70, no. 4, pp. 2450–2458, Apr. 2022.

[15] C. Ding and K.-M. Luk, "Wideband high-gain circularly polarized antenna using artificial anisotropic polarizer," *IEEE Trans. Antennas Propag.*, vol. 67, no. 10, pp. 6645–6649, Oct. 2019.
[16] T. C. Choy, *Effective Medium Theory*. Oxford, U.K.: Oxford Univ. Press, 2016.
[17] Robert Carl Yates, *A Handbook Curves their Properties*. Aylesbury, U.K.: JW Edwards, 1947.
[18] J. R. Montejo-Garai, J. A. Ruiz-Cruz, and J. M. Rebollar, "A 10-way power divider based on a transducer and a radial junction operating in the circular TM_{01} mode," *IEEE Access*, vol. 7, pp. 127353–127361, 2019.
[19] J. R. Montejo-Garai, J. A. Ruiz-Cruz, and J. M. Rebollar, "Design of radial power combiners based on TE_{01} circular waveguide mode," in *Electromagnetic Fields and Waves*. London, U.K.: IntechOpen, May 15, 2019.
[20] O. A. Peverini et al., "Selective laser melting manufacturing of microwave waveguide devices," *Proc. IEEE*, vol. 105, no. 4, pp. 620–631, Apr. 2017.
[21] C. Stoumpos, T. L. Gouguec, R. Allanic, M. García-Vigueras, and A.-C. Amiaud, "Compact additively manufactured conformal slotted waveguide antenna array," *IEEE Antennas Wireless Propag. Lett.*, vol. 22, no. 8, pp. 1843–1847, Aug. 2023.
[22] O. A. Peverini et al., "Enhanced topology of *E*-plane resonators for high-power satellite applications," *IEEE Trans. Microw. Theory Techn.*, vol. 63, no. 10, pp. 3361–3373, Oct. 2015.
[23] N. Duangrit, B. Hong, A. D. Burnett, P. Akkaraekthalin, I. D. Robertson, and N. Somjit, "Terahertz dielectric property characterization of photopolymers for additive manufacturing," *IEEE Access*, vol. 7, pp. 12339–12347, 2019.
[24] M. Forstmeier, M. Yuan, S. Perini, M. Lanagan, and B. Foley, "Dielectric characterization of paraelectric particle-loaded polymer matrix composites and commercial photoresins at W-band frequencies," *Heliyon*, vol. 9, no. 2, Feb. 2023, Art. no. e13458.
[25] A. Piroutiniya et al., "Beam steering 3D printed dielectric lens antennas for millimeter-wave and 5G applications," *Sensors*, vol. 23, no. 15, p. 6961, Aug. 2023.
[26] P. Sanchez-Olivares, E. Garcia-Marin, and J. L. Masa-Campos, "Direct metal laser sintering conformal waveguide array antenna for millimeter-wave 5G communications," *IEEE Antennas Wireless Propag. Lett.*, vol. 21, pp. 1012–1016, 2022.
[27] J. R. Montejo-Garai, J. A. Ruiz-Cruz, and J. M. Rebollar, "Evaluation of additive manufacturing techniques applied to a waveguide mode transducer," *IEEE Trans. Compon., Packag., Manuf. Technol.*, vol. 10, no. 5, pp. 887–894, May 2020.

Javier Melendro-Jiménez was born in Madrid, Spain. He received the M.Sc. degree in telecommunication engineering from the Universidad Politécnica de Madrid, Madrid, in 2022, where he is currently pursuing the Ph.D. degree.

Additionally, he currently holds the position of Antenna and RF Engineer at Airbus Defense and Space, Madrid, as well as an Associate Lecturer position with the Universidad Autónoma de Madrid. His primary interests are related with the design of antennas produced through additive manufacturing techniques, including dielectric lenses, and anisotropic polarizers.

Pablo Sanchez-Olivares was born in Madrid, Spain. He received the M.Sc. and Ph.D. degrees in telecommunication engineering from the Universidad Autónoma de Madrid, Madrid, in 2011 and 2018, respectively.

During 2019, he collaborated in Research and Development projects at the Universidad de Alcalá, Alcalá de Henares, Spain, and worked as an Adjunct Professor with the Universidad Autónoma de Madrid. In September 2019, he joined as an Assistant Professor at the Escuela Técnica Superior de Ingenieros de Telecomunicación, Universidad Politécnica de Madrid. Since April 2022, he has been an Associate Professor with the Universidad Politécnica de Madrid. His current research interests include passive and active array antennas and including design and measurement.

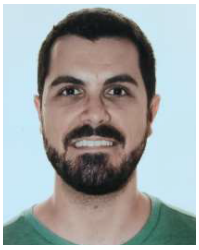

Adrián Tamayo-Domínguez was born in Madrid, Spain. He received the M.Sc. and Ph.D. degrees in telecommunication engineering from the Universidad Politécnica de Madrid (UPM), Madrid, in 2016 and 2020, respectively.

In 2017, he joined the Division of Electromagnetic Engineering and Fusion Science, School of Electrical Engineering and Computer Science, KTH Royal Institute of Technology, Stockholm, Sweeden, as a Guest Ph.D. Student. In 2020, he obtained a position as an Assistant Professor with UPM, where he continues his research activity as an Associate Professor, since 2024. His research interests include additive manufacturing, gap waveguides, and higher symmetries applied to the design of antennas.

Jose Luis Masa-Campos was born in Madrid, Spain, in 1974. He received the M.Sc. and Ph.D. degrees in telecommunication engineering from the Universidad Politécnica de Madrid (UPM), Madrid, in 1999 and 2006, respectively.

From 1999 to 2003, he developed the professional activity in the Research and Development Department of the company RYMSA with the design of base station antennas for mobile communications systems and satellite antennas, and he directed the Research and Development Department from 2002 to 2003. From 2003 to 2007, he worked as a Research Collaborator with UPM in the design of array antennas for radar and satellites systems in commercial projects for companies as INDRA or SIEMMENS. In 2005, he joined the Group of Radio Frecuency, Circuits, Antennas and Systems (RFCAS), Polytechnic College, Universidad Autonoma de Madrid (UAM), as the Chief of the Antennas Section. Since 2023, he has been an Associate Professor with the Radiation Group, UPM. His main current research interests are in design, manufacturing, measurement, and applications of planar array antennas.

Dr. Masa-Campos is a member of the National URSI Conference Organization Committee and has been the Technical Chairperson of the National URSI 2016 Conference celebrated in Madrid.

José-Manuel Fernández-González (Senior Member, IEEE) was born in Lausanne, Switzerland. He received the Diplôme d'Ingénieur en Électricité degree from the École Polytechnique Fédérale de Lausanne, Lausanne, in 2003, and the Ph.D. degree from the Universidad Politécnica de Madrid, Madrid, Spain, in 2009.

From 2006 to 2010, he got a FPU (National grant for teacher training) scholarship as a Ph.D. Student with the Universidad Politécnica de Madrid. In 2006, he joined the Center de Recherches Poly-Grames, l'École Polytechnique de Montreal, Montreal, QC, Canada, and in 2007, he joined the Chalmers University of Technology, Göteborg, Sweden, as a Guest Ph.D. Student. From 2013 to 2019, he was an Assistant Professor with the Universidad Politécnica de Madrid. In 2018, he was a Fulbright Visiting Researcher with Antenna Research Group, University of Colorado at Boulder, Boulder, CO, USA. In 2019, he got an Associate Professor with the Universidad Politécnica de Madrid. He has authored more than 100 publications in scientific journals, symposium proceedings and seminars, three book chapters and holds four patents. He has participated in more than 35 research projects and contracts. His current research interests include passive and active antennas, phased array antennas, RF circuits, and metamaterial structures.

Dr. Fernández-González is currently an Associate Editor of "IEEE ANTENNAS AND WIRELESS PROPAGATION LETTERS."